Draft version January 14, 2022
Typeset using LaTeX **twocolumn** style in AASTeX62

arXiv:1905.04900v2 [astro-ph.HE] 8 Aug 2019

Optimal neutron-star mass ranges to constrain the equation of state of nuclear matter with electromagnetic and gravitational-wave observations

L. R. Weih,[1] E. R. Most,[1] and L. Rezzolla[1]

[1] *Institut für Theoretische Physik, Goethe Universität Frankfurt am Main, Germany*

ABSTRACT

Exploiting a very large library of physically plausible equations of state (EOSs) containing more than 10^7 members and yielding more than 10^9 stellar models, we conduct a survey of the impact that a neutron-star radius measurement via electromagnetic observations can have on the EOS of nuclear matter. Such measurements are soon to be expected from the ongoing *Neutron Star Interior Composition Explorer* mission and will complement the constraints on the EOS from gravitational-wave detections. Thanks to the large statistical range of our EOS library, we can obtain a first quantitative estimate of the commonly made assumption that the high-density part of the EOS is best constrained when measuring the radius of the most massive, albeit rare, neutron stars with masses $M \gtrsim 2.1\,M_\odot$. At the same time, we find that radius measurements of neutron stars with masses $M \simeq 1.7 - 1.85\,M_\odot$ can provide the strongest constraints on the low-density part of the EOS. Finally, we quantify how radius measurements by future missions can further improve our understanding of the EOS of matter at nuclear densities.

Keywords: equation of state — gravitational waves — methods: numerical — stars: neutron

1. INTRODUCTION

The recent detection of gravitational waves (GW) from the inspiral of two neutron stars, i.e., GW170817 (Abbott et al. 2017), in combination with the observation of its electromagnetic counterpart (The LIGO Scientific Collaboration et al. 2017) has already led to a number of astrophysical constraints on the nuclear equation of state (EOS; Bauswein et al. 2017; Margalit & Metzger 2017; Paschalidis et al. 2017; Shibata et al. 2017; Abbott et al. 2018; Annala et al. 2018; Burgio et al. 2018; De et al. 2018; Fattoyev et al. 2018; Lim & Holt 2018; Malik et al. 2018; Montana et al. 2018; Most et al. 2018; Radice et al. 2018; Raithel et al. 2018; Rezzolla et al. 2018; Ruiz et al. 2018; Tews et al. 2018; Gill et al. 2019; Köppel et al. 2019; Lim & Holt 2019; Tews et al. 2019). In the near future, these constraints are expected to be complemented by precise measurements of neutron-star masses and radii via electromagnetic observations yielding constraints similar to that of a distant GW event (McNeil Forbes et al. 2019). The *Neutron Star Interior Composition Explorer* (NICER) (Arzoumanian et al. 2014; Gendreau et al. 2016) is set to deliver these constraints via X-ray modeling (see Watts et al. 2016, for a review). Anticipating these results, considerable work has been dedicated toward inferring the EOS from electromagnetic observations via Bayesian inference and different parametrizations for the EOS (Özel & Psaltis 2009; Read et al. 2009; Steiner et al. 2010; Raithel et al. 2017; Miller et al. 2019).

In this work we combine the GW constraints with possible mass and radius observations as those expected from NICER. A similar study that combines constraints has recently been undertaken by Fasano et al. (2019), who, in addition to the GW constraints, also used in their Bayesian analysis radius measurements from thermonuclear bursts in accreting neutron stars (see also Guillot et al. 2013; Lattimer & Steiner 2014; Özel et al. 2016, for earlier studies).

We here assess how much the already constrained EOS will be further restricted by precise measurements of the neutron-star radius. Greif et al. (2018) have recently shown that inferring properties of dense matter via Bayesian analysis from any astrophysical observations, i.e., from GW constraints or constraints on the neutron-star mass and radius, depends sensitively on the prior assumptions of the underlying EOS parameterization. In view of this, we do so not by relying on a Bayesian analysis or any approach involving probabilities. Rather, we consider a very large sample of EOSs whose completeness allows us to span the whole range of physically plausible EOSs given a generic and conservative parameterization. Using much smaller samples, similar approaches have already been employed in the

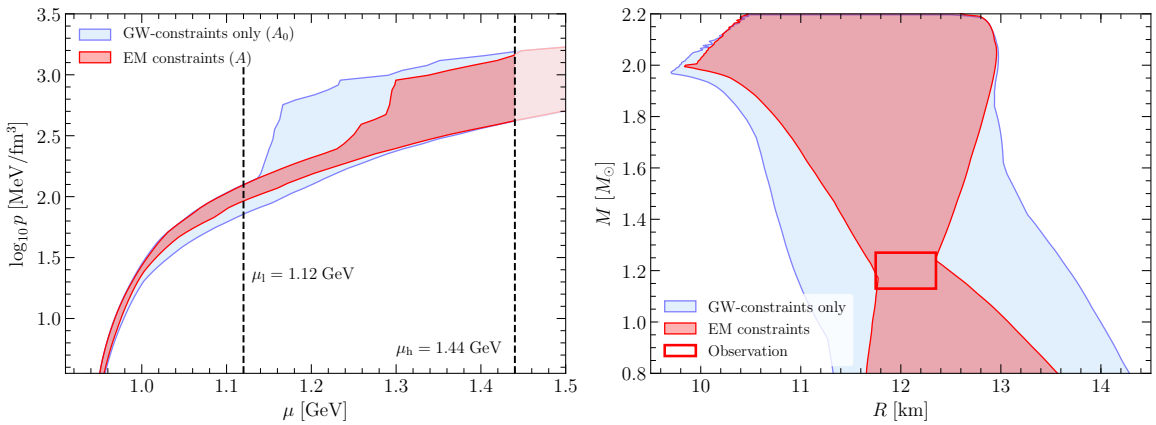


Figure 1. *Left:* areas in (p, μ) plane spanned by all EOSs fulfilling the GW constraints (light blue, A_0) and by EOSs that also fulfill a constraint as expected from an electromagnetic measurement by NICER (red, A). The dashed vertical lines limit the different ranges of the EOS in terms of the chemical potential μ. *Right:* the same areas but in the (M, R) plane. The red box marks a representative measurement by NICER. An animated version is available online (Weih et al. 2019). The animation explains our method as described in Sec. 2 graphically. It first shows how the EOSs span the areas in (p, μ) and (M, R) and then uses an examplatory radius measurement to illustrate the relation between the DOC, this measurement, and the corresponding constrained area. Finally, the animation shows how the DOC is computed for all possible radius measurements and how a color-coded representation of DOCs as the ones in Fig. 3 is generated.

past, (e.g., Hebeler et al. 2013; Kurkela et al. 2014; Annala et al. 2018), and allow for general statements that are valid independently of prior assumptions. This is true as long as the EOS sample is sufficiently large to provided convergent results as in the case of our EOS library (see also the Appendix). In this way, by considering a large set of possible outcomes of the NICER mission, we are able to assess the impact of future radius observations on our ability to further constrain the EOS and to specify the most promising mass ranges to be targeted for deriving the tightest constraints.

2. METHODS

In order to relate possible neutron-star radius measurements to the EOS, we consider equilibrium neutron-star models that are solutions to the Tolman-Oppenheimer-Volkoff (TOV) equations constructed from a comprehensive set of different EOSs obeying recent constraints from GW and kilonova observations (Most et al. 2018). These EOSs are constructed following the approach of Most et al. (2018) (see also Kurkela et al. 2014, for a similar approach), by combining state-of-the art calculations from chiral effective field theory (CEFT) (Drischler et al. 2016, 2017), describing the behavior of nuclear matter accurately close to nuclear-saturation density, together with results from perturbative QCD (pQCD) calculations (Kurkela et al. 2010; Fraga et al. 2014) for the high-density regime. We model the remaining region typically found in the core of neutron stars by parameterizing the EOS with piecewise polytropes. We only allow for EOSs that are causal, i.e., for which the speed of sound, c_s, is smaller than the speed of light, and are able to support a mass of at least $1.97\,M_\odot$ (Antoniadis et al. 2013). By matching to the pQCD limit, all of our EOSs automatically fulfill the criterion that asymptotically the sound speed is given by $c_s = \sqrt{1/3}$.

In this way, we have constructed a set of $\simeq 2.5 \times 10^7$ physically plausible EOSs from which we have computed $\simeq 3.8 \times 10^9$ stellar models. All of our EOSs are purely hadronic and hence do not account for a first-order phase transition. While this is a limitation that we will address in a future work, stellar models with phase transitions have been found to represent a small fraction of the physically plausible EOSs (Most et al. 2018). To this set, which we refer to as the *"complete"* set, we apply the constraints derived from the GW event GW170817 (Abbott et al. 2017; Abbott et al. 2018). These constraints have been derived in several works and can be summarized as follows:

(i) The maximum mass reached by a sequence of non-rotating neutron stars does not exceed $\simeq 2.2\,M_\odot$ (Margalit & Metzger 2017; Shibata et al. 2017; Rezzolla et al. 2018; Ruiz et al. 2018). This is a conservative value for the maximum mass that agrees with the error bounds of the four papers listed above. We also compare our results to the case of a higher value for this upper limit, i.e., $\simeq 2.3\,M_\odot$, as suggested in Shibata et al. (2019) and in agreement with the upper bound of Rezzolla et al. (2018). A discussion in the Appendix will illustrate how a different choice of the maximum mass impacts our results only marginally.

(ii) The tidal deformability of a $1.4\,M_\odot$ star, $\Lambda_{1.4}$, is constrained to be in the range $290 < \Lambda_{1.4} < 580$, where the upper limit is the observational constraint from GW170817 (Abbott et al. 2018), while the lower limit is deduced from the analysis of Most et al. (2018) and is consistent with a number of other studies (Abbott et al. 2018; Coughlin et al. 2018; De et al. 2018; Kiuchi et al. 2019).

Imposing these constraints reduces our set of EOSs considerably, leaving us with $\approx 20\,\%$ of the complete set. We refer to this reduced library as the *"constraint-satisfying"* set and it is marked with the light blue area in Fig. 1, whose left panel provides a representation in the pressure-chemical potential plane, (p, μ), while the right panel in the mass-radius plane (M, R).

A number of remarks are useful at this point. First, it is essential that the sample of EOSs considered is sufficiently large so as to provide a robust statistical representation after the GW constraints are imposed. We have verified that this is the case by considering sets of 2.5, 1.5, and 1.0×10^7 EOSs, which all provide the same statistical results. Second, the evidence that the GW constraints remove about $80\,\%$ of the physically plausible EOSs, underlines the importance of a sufficiently large sample of EOSs that allows for convergent results (see the discussion in the Appendix). Third, several works have also derived constraints on the radius of a $1.4\,M_\odot$ star (Annala et al. 2018; Burgio et al. 2018; De et al. 2018; Malik et al. 2018; Most et al. 2018; Raithel et al. 2018; Tews et al. 2018); these constraints are compatible with our range of admissible tidal deformabilities. Fourth, the range for $\Lambda_{1.4}$ is also in agreement with constraints stemming from the threshold mass to prompt collapse (Bauswein et al. 2017; Köppel et al. 2019). Finally, Gamba et al. (2019) have recently shown that while the constraints on the radius might sensitively depend on the description of the EOS for the neutron-star crust, the constraints on $\Lambda_{1.4}$ are more robust.

To quantify how well potential observations of neutron-star radii can further constrain the EOS in addition to the constraints already imposed, we need to define a measure of the degree to which an EOS is constrained. More specifically, because the pressure $p(\mu)$ is a thermodynamical potential that fully describes the EOS at $T = 0$, we consider as a reference measure of the properties of our EOS library the area spanned by the constraint-satisfying set of EOSs in our sample, i.e.,

$$A_0 \coloneqq \int d\mu \int dp(\mu) = \int_0^{\mu_\mathrm{h}} [\max(p(\mu)) - \min(p(\mu))]\, d\mu\,, \tag{1}$$

where the maximum and minimum in the integral is taken at each point μ and over the set of constraint-satisfying EOSs. We choose $\mu_\mathrm{h} = 1.44\,\mathrm{GeV}$ which is the largest chemical potential found in our constraint-satisfying sample and reflects the fact that neutron stars cannot probe the EOS beyond the largest densities found in their cores (the highest number density in our sample is $\sim 6.5\,n_0$, where $n_0 = 0.16\,\mathrm{fm}^{-3}$ is the nuclear-saturation density). Note that by varying the range in the chemical potential over which the integral in Eq. (1) is performed we can probe in a differential manner the low-density and the high-density regimes of the EOS. In particular, we will define the low (high)-density reference areas $A_{0,\mathrm{l}}$ ($A_{0,\mathrm{h}}$) if the integral (1) is instead performed in the range $[0, \mu_\mathrm{l}]$ ($[\mu_\mathrm{l}, \mu_\mathrm{h}]$), where $\mu_\mathrm{l} = 1.12\,\mathrm{GeV}$[1] (see black dashed lines in Fig. 1).

Having defined a reference area A_0, we can ask how it changes when we impose an additional constraint from a hypothetical mass and radius measurement. For simplicity we represent such an observation in terms of a square box in the (M, R) plane whose boundaries are determined by the errors of the measurement. Any EOS not passing through this box can then be discarded as being in disagreement with the observation. An illustration of this logic is shown in Fig. 1, where the new area A is represented by the red-shaded area and where a hypothetical measurement has been made of a neutron star with mass $1.2 \pm 0.07\,M_\odot$ and radius $12.0 \pm 0.3\,\mathrm{km}$ (red box in Fig. 1). In this way, we can measure the *"degree of constraint"* (DOC) of the observation simply as

$$\chi \coloneqq 1 - \frac{A}{A_0}\,, \tag{2}$$

where $\chi \ll 1$ refers to a measurement that is not constraining the EOS appreciably, while $\chi \simeq 1$ would indicate a measurement that can set significant constraints on the EOS, as when the red-shaded area in Fig. 1 shrinks to a line. In logical analogy with the definition of (2), we can measure the DOCs for the low (high)-density region of the EOS, χ_l (χ_h), by simply replacing A and A_0 with the corresponding areas computed when $\mu \in [0, \mu_\mathrm{l}]$ ($[\mu_\mathrm{l}, \mu_\mathrm{h}]$).

Using these definitions, we can now assess how well a given mass/radius measurement would constrain the EOS and, more importantly, which part of the EOS is actually constrained. Before doing that, however, we underline that the DOC, χ, depends on the prior with which the EOSs are constructed. As long as the EOS sample size is large enough, however, all DOCs computed with any prior will converge to the same value.

[1] This value corresponds roughly to where we match the EOS from CEFT. Since the matching is done at a fixed number density, it corresponds to different values of μ for each EOS.

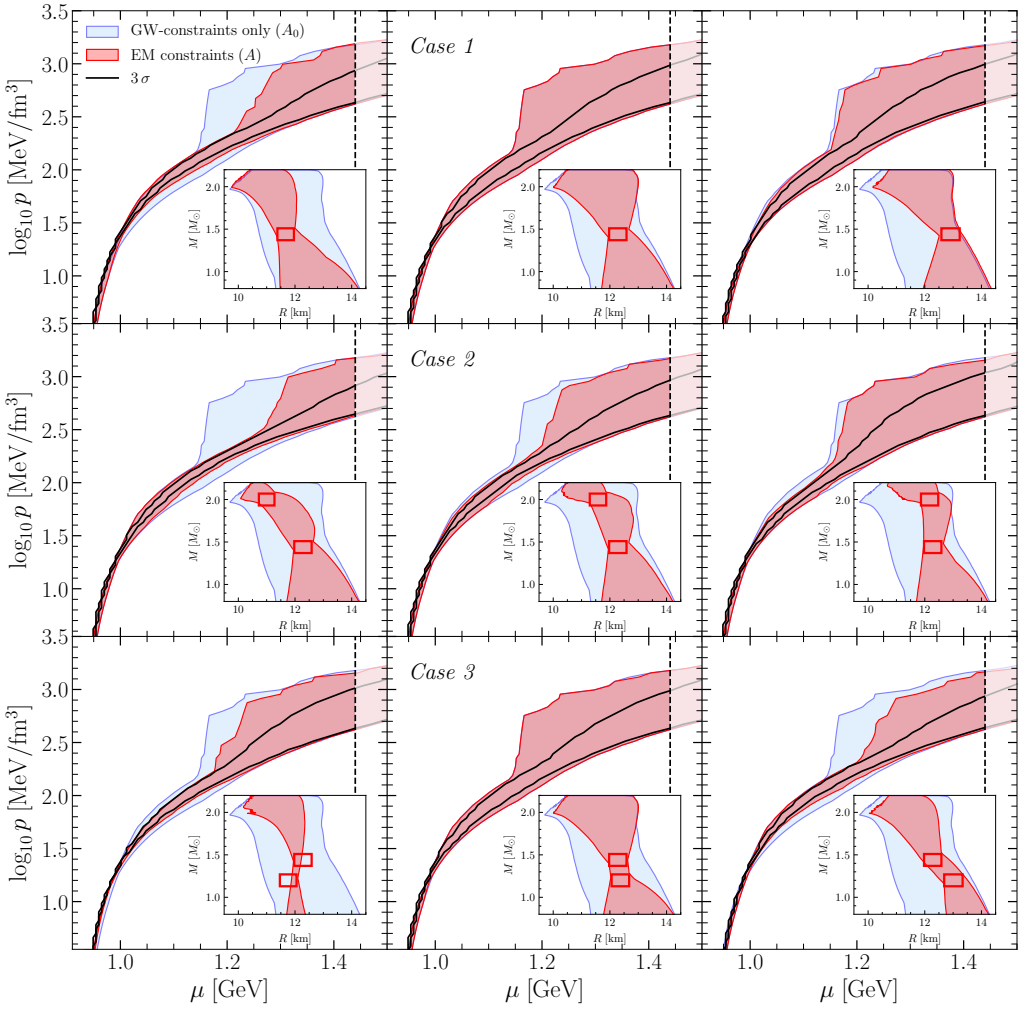


Figure 2. Same as in Fig. 1 but specialized to the reference *Case 1*-*Case 3* in the text. For each row the central column refers to radius measurements inferred by Most et al. (2018), while the left/right columns explore the cases when the radius is 10% smaller/larger. Shown with solid black lines in each panel are the $3\,\sigma$ confidence levels obtained from a Bayesian analysis of the EOS distributions.

This is an important added value of our approach compared with other works.

3. RESULTS

Hereafter, we will consider three main cases that are believed to be possible outcomes of the NICER mission (Arzoumanian et al. 2014; Watts et al. 2016), namely (see also Greif et al. 2018, for similar choices):

Case 1: Only one of the primary targets, i.e., PSR J0437-4715, with a mass of $1.44\,M_\odot$ will be successfully measured yielding a radius of 12.28 ± 0.31 km.

Case 2: Both primary targets, i.e., PSR J0437-4715 and PSR J0030+0451 will be successfully measured. For the latter the mass is unknown and we here consider a massive star with $2.0\,M_\odot$ with the same error as for PSR J0437-4715. For the radius we assume 11.58 ± 0.29 km.

Case 3: The same as *Case 2*, but with $1.2\,M_\odot$ for PSR J0030+0451 and a radius of 12.37 ± 0.31 km.

The radii in the cases above are taken as the most likely values reported by Most et al. (2018), together with a 5 % relative error on the radius (Arzoumanian et al. 2014) and a fixed uncertainty of $\pm 0.07\,M_\odot$ for the mass[2], where the latter is motivated by the typical accuracy of known neutron-star masses (Özel & Freire 2016).

Shown in the middle panel of the first row of Fig. 2 is a graphical representation of how the DOC is defined, i.e., as the ratio of the red to the blue area. This panel shows these areas for *Case 1* (shown in the inset are the corresponding areas in the (M, R) plane).

[2] For a larger error of $\pm 0.14\,M_\odot$, or 10 % uncertainty in the radius measurement, we obtain essentially the same results, with slightly smaller values for the DOCs.

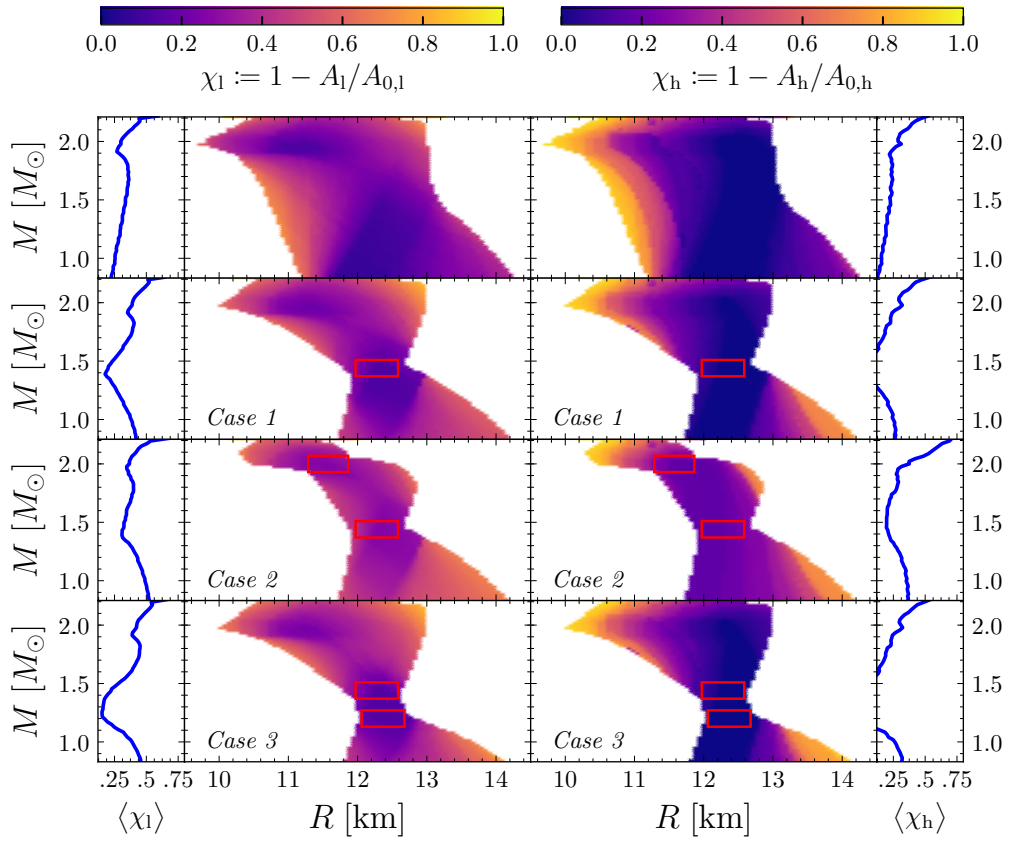


Figure 3. Degrees of constraint (DOCs) in the (M, R) plane for the low- (left panels, $\chi_{\rm l}$) and high-density (right panels, $\chi_{\rm h}$) regions of the EOS and for all possible hypothetical observations. We assume the constraint of such an observation in addition to already existing constraints. The top row refers to GW constraints only, while the other rows refer to an assumed outcome of the NICER mission (red boxes), i.e., *Case 1*-*Case 3*, respectively. The left and right side panels show the radius-averaged DOCs, $\langle\chi_{\rm l,h}\rangle$.

Note that in this case $\chi \simeq 0$ as the blue- and red-shaded areas essentially coincide, thus indicating that a measurement of this type would constrain the EOS only marginally. Similar considerations apply also when examining a measured radius that is 10 % larger, as indicated in the top right panel of Fig. 2. On the other hand, the top left panel, which refers to a measured radius that is 10 % smaller, shows that $\chi \sim 0.67$, thus indicating that measuring a compact star would provide important constraints on the EOS. Stated differently, given a $1.44\,M_\odot$ star, the most significant constraints on the EOS would be obtained if the star had a radius $R_{1.44} \lesssim 12\,$km.

Similar conclusions follow also for *Cases 2* and *3*, which are reported, respectively, in the central panel of rows two and three of Fig. 2, while the corresponding left/right panels refer to the same cases, but assuming a smaller/larger radius for PSR J0030+0451. As a reference, we also show with black solid lines the $3\,\sigma$ confidence levels obtained by computing the probability distribution function (PDF) via a Bayesian analysis where we use the maximum of a bivariate Gaussian distribution within the red box in the (M, R) plane for the likelihoods (as done in, e.g., Raithel et al. 2017), and the PDF obtained by Most et al. (2018) as prior. The area encompassed by these lines shows that even when $\chi \simeq 0$, constraints on the EOS may still be obtained within a given confidence level. In particular, for the high-density part of the EOS the $3\,\sigma$ confidence intervals remain unchanged under various radius measurements. Because the precise measure of these constraints will depend upon the choice of prior used for the Bayesian analysis (Greif et al. 2018), we will here use the DOC defined in Eq. (2), which is free of this bias as it only compares the outer limits of the EOS space covered, for which we can show convergence irrespective of the prior.

The first row of Fig. 3 shows with a colorcode for each point in the (M, R) plane the DOC when an observational box is centered around that point. In other words, we consider the DOC for all possible mass/radius

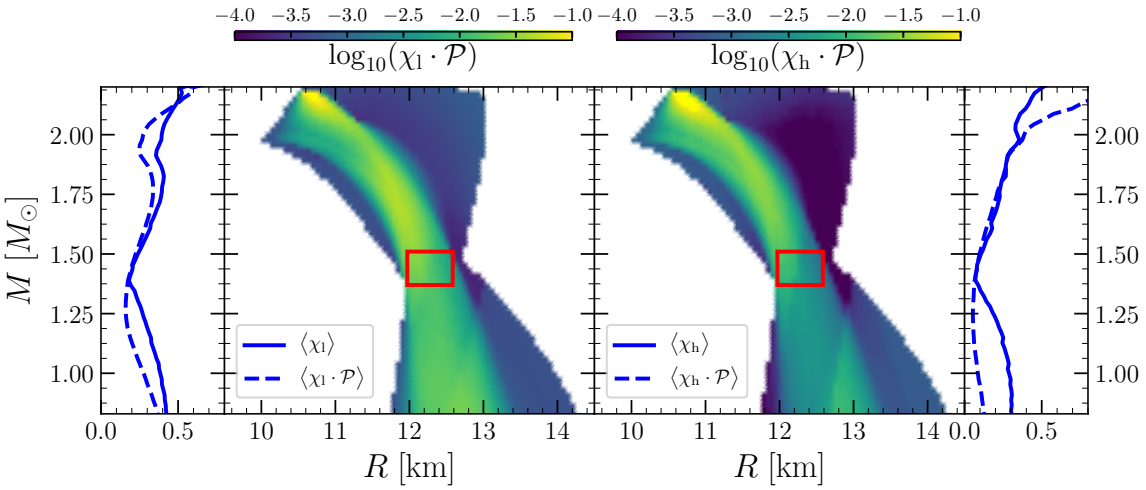


Figure 4. Same as in the second row of Fig. 3 (*Case 1*), but showing the probability-weighted DOCs, $\chi_{\rm l,h}\cdot\mathcal{P}$. The left and right side panels show the corresponding deconvolved and radius-averaged DOCs, $\langle\chi_{\rm l,h}\cdot\mathcal{P}\rangle$.

measurements. Note that we now distinguish the DOCs relative to the low- (left panel) and high-density (right panel) regions of the EOS. Obviously, an observation providing a box at the edges of the area spanned in the (M, R) plane would provide the best constraints as the underlying EOSs there are the scarcest. The left and right side columns of Fig. 3 show with blue lines the averaged DOCs $\langle\chi_{\rm l,h}\rangle$, namely, the radial averages of $\chi_{\rm l}$ and $\chi_{\rm h}$ taken at a fixed mass. It is then evident that the best constraints on the EOS can be expected from measuring the radius of a neutron star that is as massive as possible, because these stars have densities in their cores for which the EOS is least known. Interestingly, Fig. 3 also shows that there is a local maximum for $\langle\chi_{\rm l}\rangle$ around $M\sim1.8\,M_\odot$, thus suggesting that – apart from very massive and rare stars with $M\gtrsim2.1\,M_\odot$ – a radius measurement in the range of $1.7-1.85\,M_\odot$ would yield the best constraints on the low-density regime of the EOS. While this is true only on average and the DOC will depend on the exact measured value, this is the first time that such an evidence is found. We also remark that if going to higher masses yields smaller DOCs, this is most likely due to the presence of a lower limit on the maximum mass $M_{\rm TOV}>1.97M_\odot$.

The last three rows of Fig. 3 show the same DOCs for *Case 1-3* and hence describe the degree to which the EOS is constrained for an additional radius measurement beyond NICER. In all three cases, the local maximum around $\sim1.8\,M_\odot$ is again present for $\langle\chi_{\rm l}\rangle$, underlining the importance that a star in this mass range would have on constraining the low-density regime of the EOS.

The averaged DOCs $\langle\chi_{\rm l,h}\rangle$ seem to suggest that the EOS would be considerably constrained also for a radius measurement of a star with $M\lesssim1.1\,M_\odot$, thus making low-mass stars almost as promising as the high-mass ones. Such large averaged DOCs are the results of the increase in $\chi_{\rm h}$ following the measurement of a low-mass star with a large radius (i.e., $\gtrsim13.5$ km; see the orange part of the right panels for $\chi_{\rm h}$ in Fig. 3). In practice, however, such large DOCs do not take into account that in our library a large radius for such low-mass stars is rare and hence unlikely to be observed. This can be countered by convolving the DOC with the PDF $\mathcal{P}$ of encountering a star with a given mass and radius. While a trivial step to take given that we already have this information (Most et al. 2018), it also introduces a new direct dependency on the prior used in building the set of EOSs, and would sacrifice the general validity of our results.

Notwithstanding this, we report in Fig. 4 the result of such weighting and show the PDF-weighted DOCs, $\chi_{\rm l,h}\cdot\mathcal{P}$, and the averaged PDF-weighted DOCs, $\langle\chi_{\rm l,h}\cdot\mathcal{P}\rangle$, for *Case 1*, with the PDF here being the same as that used for the computation of the $3\,\sigma$ lines in Fig. 2. In this way, we learn that while large DOCs $\langle\chi_{\rm l,h}\rangle$ for a $1.8\,M_\odot$ star are robust, this is not the case for a low-mass star with mass $\lesssim1.1\,M_\odot$. This is particularly evident for the high-density part of the EOS, for which $\langle\chi_{\rm h}\cdot\mathcal{P}\rangle\ll\langle\chi_{\rm h}\rangle$. We find this behavior in all scenarios: while a large $\chi_{\rm l}$ is robust and indicative of a genuine high DOC, a large $\chi_{\rm h}$ at low masses may need to be weighted by the probability of finding stars in this mass range with such extreme radii.

4. CONCLUSIONS

We have presented an extensive survey of how electromagnetic measurements of masses and radii of neutron stars, when combined with the constraints from GW170817, will provide information on the EOS of nuclear matter. Our findings confirm the expectation that radius measurements of stars with masses $M \gtrsim 2.0\,M_\odot$ represent the most effective manner of setting constraints on the highest-density regimes of the EOS. At the same time, our analysis reveals the existence of an optimal mass range of $M \sim 1.7 - 1.85\,M_\odot$, which would yield the best constraints on the low-density regime of the EOS with observations beyond those made by the NICER mission. Finally, low-mass stars with $M \lesssim 1.1\,M_\odot$, could also provide significant constraints on the low-density regime of the EOS.

The library of EOSs and stellar models presented here and providing a convergent and complete coverage of physically plausible EOSs, is publicly available online [3] (Weih et al. 2019) and can be used as new GW detections of merging neutron-star binaries or mass/radius measurements become available. Such detections can be employed to provide even more stringent constraints on the properties of the EOS of nuclear matter. The library will also be updated to incorporate phase transitions and new observational constraints, such as those on the maximum mass via the binary system PSR J0740+6620 (Thankful Cromartie et al. 2019).

ACKNOWLEDGEMENTS

It is a pleasure to thank Cole Miller, Cecilia Chirenti and Anna Watts for useful discussions. Support comes also in part from HGS-HIRe for FAIR; the LOEWE-Program in HIC for FAIR; "PHAROS", COST Action CA16214 European Union's Horizon 2020 Research and Innovation Programme (grant 671698) (call FETHPC-1-2014, project ExaHyPE); the ERC Synergy Grant "BlackHoleCam: Imaging the Event Horizon of Black Holes" (grant No. 610058).The calculations were performed on the GOETHE cluster at CSC in Frankfurt.

APPENDIX

In this Appendix we provide additional information on some of the issues discussed in the main text.

We start with providing convincing evidence that our results have been obtained with a sufficiently large sample of EOSs to be statistically robust and significant. In particular, the convergence of our results is reported in Fig. 5, which highlights the importance of having a large enough sample of EOSs for reaching convergent results. With smaller samples it is of course still possible to obtain statistical results via, e.g., Bayesian analysis. For results over the whole range of physically plausible EOSs, however, we find that at least $\sim 5 \times 10^6$ EOSs are necessary for our parameterization to populate also the rare EOSs at the very stiff and soft ends of the spectrum. This is mostly necessary because the largest part of our sample, i.e., $\sim 80\%$ of it, is excluded after applying the GW constraints and it is further reduced when applying the constraints from a hypothetical radius measurement.

Next, we show that our results are robust with respect to the precise value chosen for the upper limit on the maximum mass $M_{\rm TOV}$. Although the value of $M_{\rm TOV} \lesssim 2.2\,M_\odot$ is in agreement with a number of studies each using different methods (Margalit & Metzger 2017; Shibata et al. 2017; Rezzolla et al. 2018; Ruiz et al. 2018), it has recently been argued that this upper limit might be higher and that it is weakly constrained to be $M_{\rm TOV} \lesssim 2.3\,M_\odot$ (Shibata et al. 2019) which is consistent with the upper uncertainty bound provided by Rezzolla et al. (2018), namely, $M_{\rm TOV} \lesssim 2.16^{+0.17}_{-0.15}\,M_\odot$. To assess the validity of our results we report in Fig. 6 the changes in the DOCs when considering this higher value. As it can be deduced clearly when comparing the results in the top ($M_{\rm TOV} < 2.2\,M_\odot$) and bottom panels ($M_{\rm TOV} < 2.3\,M_\odot$) of Fig. 6, the impact of considering a larger maximum mass is only marginal. More importantly, the evidence that the mass range around $M \sim 1.8\,M_\odot$ provides the optimal constraint for $\langle \chi_{\rm l} \rangle$ remains unchanged.

[3] 10.5281/zenodo.3260991

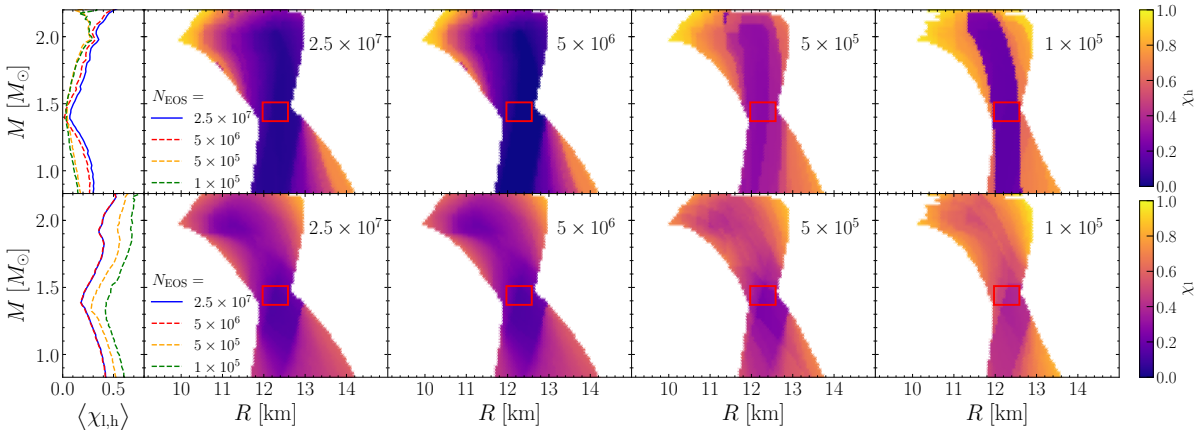


Figure 5. Same as the second row in Fig. 3, but for different sizes of our EOS sample. From left to right we compare the results for samples of size 2.5×10^7 (blue), 5×10^6 (red), 5×10^5 (yellow), and 1×10^5 (green).

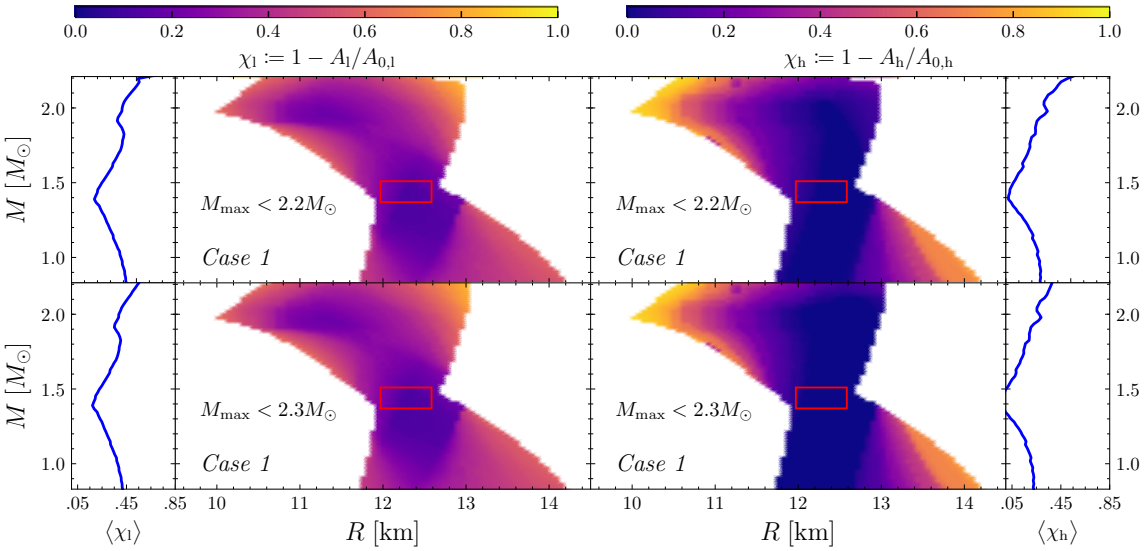


Figure 6. Same as the second row in Fig. 3, but when using different values for the upper limit on $M_{\rm TOV}$. The top and bottom panels show the results for $M_{\rm TOV} < 2.2\,M_\odot$ and $M_{\rm TOV} < 2.3\,M_\odot$, respectively.

REFERENCES

Abbott, B. P., et al. 2017, Phys. Rev. Lett., 119, 161101, doi: 10.1103/PhysRevLett.119.161101

Abbott, B. P., Abbott, R., Abbott, T. D., et al. 2018, Physical Review Letters, 121, 161101, doi: 10.1103/PhysRevLett.121.161101

Annala, E., Gorda, T., Kurkela, A., & Vuorinen, A. 2018, Phys. Rev. Lett., 120, 172703, doi: 10.1103/PhysRevLett.120.172703

Antoniadis, J., Freire, P. C. C., Wex, N., et al. 2013, Science, 340, 448, doi: 10.1126/science.1233232

Arzoumanian, Z., Gendreau, K. C., Baker, C. L., et al. 2014, in Proc. SPIE, Vol. 9144, Space Telescopes and Instrumentation 2014: Ultraviolet to Gamma Ray, 914420, doi: 10.1117/12.2056811

Bauswein, A., Just, O., Janka, H.-T., & Stergioulas, N. 2017, Astrophys. J. Lett., 850, L34, doi: 10.3847/2041-8213/aa9994

Burgio, G. F., Drago, A., Pagliara, G., Schulze, H.-J., & Wei, J.-B. 2018, Astrophys. J., 860, 139, doi: 10.3847/1538-4357/aac6ee

Coughlin, M. W., Dietrich, T., Margalit, B., & Metzger, B. D. 2018, arXiv e-prints. https://arxiv.org/abs/1812.04803

De, S., Finstad, D., Lattimer, J. M., et al. 2018, ArXiv e-prints. https://arxiv.org/abs/1804.08583

Drischler, C., Carbone, A., Hebeler, K., & Schwenk, A. 2016, Phys. Rev. C, 94, 054307, doi: 10.1103/PhysRevC.94.054307

Drischler, C., Hebeler, K., & Schwenk, A. 2017, ArXiv e-prints. https://arxiv.org/abs/1710.08220

Fasano, M., Abdelsalhin, T., Maselli, A., & Ferrari, V. 2019, arXiv e-prints. https://arxiv.org/abs/1902.05078

Fattoyev, F. J., Piekarewicz, J., & Horowitz, C. J. 2018, Physical Review Letters, 120, 172702, doi: 10.1103/PhysRevLett.120.172702

Fraga, E. S., Kurkela, A., & Vuorinen, A. 2014, Astrophys. J. Lett., 781, L25, doi: 10.1088/2041-8205/781/2/L25

Gamba, R., Read, J. S., & Wade, L. E. 2019, arXiv e-prints. https://arxiv.org/abs/1902.04616

Gendreau, K. C., Arzoumanian, Z., Adkins, P. W., et al. 2016, in Proc. SPIE, Vol. 9905, Space Telescopes and Instrumentation 2016: Ultraviolet to Gamma Ray, 99051H, doi: 10.1117/12.2231304

Gill, R., Nathanail, A., & Rezzolla, L. 2019, Astrophys. J., in press. https://arxiv.org/abs/1901.04138

Greif, S. K., Raaijmakers, G., Hebeler, K., Schwenk, A., & Watts, A. L. 2018, arXiv e-prints. https://arxiv.org/abs/1812.08188

Guillot, S., Servillat, M., Webb, N. A., & Rutledge, R. E. 2013, Astrophys. J., 772, 7, doi: 10.1088/0004-637X/772/1/7

Hebeler, K., Lattimer, J. M., Pethick, C. J., & Schwenk, A. 2013, Astrophys. J., 773, 11, doi: 10.1088/0004-637X/773/1/11

Kiuchi, K., Kyutoku, K., Shibata, M., & Taniguchi, K. 2019, arXiv e-prints, arXiv:1903.01466. https://arxiv.org/abs/1903.01466

Köppel, S., Bovard, L., & Rezzolla, L. 2019, Astrophys. J. Lett., 872, L16, doi: 10.3847/2041-8213/ab0210

Kurkela, A., Fraga, E. S., Schaffner-Bielich, J., & Vuorinen, A. 2014, Astrophys. J., 789, 127, doi: 10.1088/0004-637X/789/2/127

Kurkela, A., Romatschke, P., & Vuorinen, A. 2010, Phys. Rev. D, 81, 105021, doi: 10.1103/PhysRevD.81.105021

Lattimer, J. M., & Steiner, A. W. 2014, Astrophys. J., 784, 123, doi: 10.1088/0004-637X/784/2/123

Lim, Y., & Holt, J. W. 2018, Physical Review Letters, 121, 062701, doi: 10.1103/PhysRevLett.121.062701

—. 2019, arXiv e-prints. https://arxiv.org/abs/1902.05502

Malik, T., Alam, N., Fortin, M., et al. 2018, PhRvC, 98, 035804, doi: 10.1103/PhysRevC.98.035804

Margalit, B., & Metzger, B. D. 2017, Astrophys. J. Lett., 850, L19, doi: 10.3847/2041-8213/aa991c

McNeil Forbes, M., Bose, S., Reddy, S., et al. 2019, arXiv e-prints. https://arxiv.org/abs/1904.04233

Miller, M. C., Chirenti, C., & Lamb, F. K. 2019, arXiv e-prints, arXiv:1904.08907. https://arxiv.org/abs/1904.08907

Montana, G., Tolos, L., Hanauske, M., & Rezzolla, L. 2018. https://arxiv.org/abs/1811.10929

Most, E. R., Weih, L. R., Rezzolla, L., & Schaffner-Bielich, J. 2018, Phys. Rev. Lett., 120, 261103, doi: 10.1103/PhysRevLett.120.261103

Özel, F., & Freire, P. 2016, Annual Review of Astronomy and Astrophysics, 54, 401, doi: 10.1146/annurev-astro-081915-023322

Özel, F., & Psaltis, D. 2009, Phys. Rev. D, 80, 103003, doi: 10.1103/PhysRevD.80.103003

Özel, F., Psaltis, D., Güver, T., et al. 2016, Astrophys. J., 820, 28, doi: 10.3847/0004-637X/820/1/28

Paschalidis, V., Yagi, K., Alvarez-Castillo, D., Blaschke, D. B., & Sedrakian, A. 2017, arXiv:1712.00451. https://arxiv.org/abs/1712.00451

Radice, D., Perego, A., Zappa, F., & Bernuzzi, S. 2018, Astrophys. J. Lett., 852, L29, doi: 10.3847/2041-8213/aaa402

Raithel, C., Özel, F., & Psaltis, D. 2018, Astrophys. J., 857, L23, doi: 10.3847/2041-8213/aabcbf

Raithel, C. A., Özel, F., & Psaltis, D. 2017, Astrophys. J., 844, 156, doi: 10.3847/1538-4357/aa7a5a

Read, J. S., Lackey, B. D., Owen, B. J., & Friedman, J. L. 2009, Phys. Rev. D, 79, 124032, doi: 10.1103/PhysRevD.79.124032

Rezzolla, L., Most, E. R., & Weih, L. R. 2018, Astrophys. J. Lett., 852, L25, doi: 10.3847/2041-8213/aaa401

Ruiz, M., Shapiro, S. L., & Tsokaros, A. 2018, Phys. Rev. D, 97, 021501, doi: 10.1103/PhysRevD.97.021501

Shibata, M., Fujibayashi, S., Hotokezaka, K., et al. 2017, Phys. Rev. D, 96, 123012, doi: 10.1103/PhysRevD.96.123012

Shibata, M., Zhou, E., Kiuchi, K., & Fujibayashi, S. 2019, arXiv e-prints, arXiv:1905.03656. https://arxiv.org/abs/1905.03656

Steiner, A. W., Lattimer, J. M., & Brown, E. F. 2010, Astrophys. Journ., 722, 33, doi: 10.1088/0004-637X/722/1/33

Tews, I., Margueron, J., & Reddy, S. 2018, Physical Review C, 98, 045804, doi: 10.1103/PhysRevC.98.045804

—. 2019, arXiv e-prints. https://arxiv.org/abs/1901.09874

Thankful Cromartie, H., Fonseca, E., Ransom, S. M., et al. 2019, arXiv e-prints, arXiv:1904.06759. https://arxiv.org/abs/1904.06759

The LIGO Scientific Collaboration, the Virgo Collaboration, Abbott, B. P., et al. 2017, Astrophys. J. Lett., 848, L12. http://stacks.iop.org/2041-8205/848/i=2/a=L12

Watts, A. L., Andersson, N., Chakrabarty, D., et al. 2016, Reviews of Modern Physics, 88, 021001, doi: 10.1103/RevModPhys.88.021001

Weih, L. R., Most, E. R., & Rezzolla, L. 2019, Optimal neutron-star mass ranges to constrain the equation of state of nuclear matter with electromagnetic and gravitational-wave observations: Animated Fig. 1, 1.0, Zenodo, doi: 10.5281/zenodo.3363615

Weih, L. R., Most, E. R., & Rezzolla, L. 2019, Optimal neutron-star mass ranges to constrain the equation of state of nuclear matter with electromagnetic and gravitational-wave observations: EOS library, 1.0, Zenodo, doi: 10.5281/zenodo.3260991